UC San Diego
UC San Diego Electronic Theses and Dissertations

Title
Global Distribution and Morphology of Small Seamounts

Permalink
https://escholarship.org/uc/item/7008q65n

Author
Gevorgian, Julie Mary

Publication Date
2022

Peer reviewed|Thesis/dissertation

UNIVERSITY OF CALIFORNIA SAN DIEGO

Global Distribution and Morphology of Small Seamounts

A thesis submitted in partial satisfaction of the
requirements for the degree Master of Science

in

Earth Sciences

by

Julie Gevorgian

Committee in charge:

       Professor David Sandwell, Chair
       Professor Jeffrey Gee
       Professor Ross Parnell-Turner

2022

The thesis of Julie Gevorgian is approved, and it is acceptable in quality and form for publication on microfilm and electronically.

University of California San Diego

2022

DEDICATION

To my Family

To Hrant and Mary Papazian

TABLE OF CONTENTS

LIST OF FIGURES

LIST OF TABLES

ACKNOWLEDGEMENTS

I would like to acknowledge Professor David Sandwell for his support as the chair of my committee. Thank you for giving me the opportunity and providing me with a space where I could contribute to and expand my understanding of Earth Science. Your guidance allowed me to grow as a student and challenge myself as a researcher. I could not have asked for a better mentor.

I would also like to acknowledge and thank Professor Jeffrey Gee and Professor Ross Parnell-Turner for being part of my thesis committee. Thank you to the Sandwell lab for welcoming me openly and listening to my weekly updates since the day I started on my research. Thank you to Yao Yu, who was always there to help me with my scripts. Your kindness and encouragement throughout the process will forever be appreciated.

ABSTRACT OF THE THESIS

Global Distribution and Morphology of Small Seamounts

by

Julie Gevorgian

Master of Science in Earth Sciences

University of California San Diego, 2022

Professor David Sandwell, Chair

Seamounts are isolated elevations in the seafloor with circular or elliptical plans, comparatively steep slopes, and relatively small summit areas (*Menard*, 1964). The vertical gravity gradient (VGG), which is the curvature of the ocean surface topography derived from satellite altimeter measurements, has been used to map the global distribution of seamounts (*Kim and Wessel*, 2011). We used the latest grid of VGG to update and refine the global seamount catalog; we identified 10,796 new seamounts, expanding the catalog by 1/3. 739 well-surveyed seamounts, having heights ranging from 421 m to 2500 m, were then used to estimate the typical radially-symmetric seamount morphology. First, an Empirical Orthogonal Function (EOF) analysis was used to demonstrate that these small seamounts have a basal radius that is linearly related to

their height – their shapes are scale invariant. Two methods were then used to compute this characteristic base to height ratio: an average Gaussian fit to the stack of all profiles and an individual Gaussian fit for each seamount in the sample. The first method combined the radial normalized height data from all 739 seamounts to form median and median-absolute deviation. These data were fitted by a 3-parameter Gaussian model that explained 99.82 percent of the variance. The second method used the Gaussian function to individually model each seamount in the sample and further establish the Gaussian model. Using this characteristic Gaussian shape, we show that VGG can be used to estimate the height of small seamounts to an accuracy of about 270 m.

Chapter 1

Introduction

1.1   What are Seamounts?

The ocean floor consists of primary tectonic features that form at spreading ridges including abyssal hills, transform faults, and propagating ridges as well as seamounts that form away from the ridges. Seamounts are active or extinct volcanoes with heights that reach at least 1000 meters (*Menard*, 1964), although this definition has been broadened to include much smaller isolated volcanoes (*Staudigel et al.*, 2010). They are basaltic in composition, volcanic in origin, and formed in one of three tectonic settings: near mid-ocean ridges, intraplate hotspots, and island arcs (*Wessel et al.*, 2010). (1) The majority of seamounts form near mid-ocean ridges. The lithosphere at divergent plate boundaries is thin and fractured allowing for magma to propagate through the lithosphere and form small seamounts that are tens to thousands of meters high (*Batiza*, 1981; *Smith and Cann*, 1990). (2) Intraplate seamounts that form away from the spreading ridges, usually on older seafloor, are generally attributed to hotspots (*Vogt*, 1974). The hotspot hypothesis states that as the plate passes over a relatively stationary mantle upwelling (i.e., plume), melt generated at the lithosphere/asthenosphere migrates to the surface, thus forming an age-progressive seamount chain (*Wilson*, 1963; *Morgan*, 1971). (3) Island arc seamounts form in the overriding plate at subduction zones. When the oceanic crust of the subducting plate reaches a depth of about 150 km, the basalt transforms to eclogite and releases water that lowers the melting temperature in the mantle wedge that erupts, forming island arc

volcanoes (*Fryer*, 1996).

The means of formation also has an effect on seamount size and distribution. For one, flanks of spreading centers tend to have many small seamounts (less than 3 km tall) since the lithosphere is thin (*Batiza*, 1981). However, if a seamount is created by a mantle plume beneath thick lithosphere, it can reach a peak of 3 - 10 km above the seafloor (*Wessel*, 2007). The distribution of seamounts differs among ocean basins and this variation can be due to the distribution of mantle plumes as well as changes in intraplate stresses. The global distribution of seamounts height follows an exponential or a power-law model (*Smith and Jordan*, 1988; *Wessel*, 1997, 2001). This model suggests that the majority of seamounts are small and there could be 50 to 100 thousand seamounts with heights above 1 km (*Wessel*, 2007; *Kim and Wessel*, 2011). Therefore, there is an age to size relationship in seamounts; smaller seamounts generally form on young, thin lithosphere, while larger seamounts generally form on older, thicker lithosphere (*Vogt*, 1974; *Watts et al.*, 2006).

The knowledge of the global distribution of seamounts is still incomplete because only 20 percent of the seafloor has been mapped by ships (*Mayer et al.*, 2018). However, seamounts are valuable characteristics of the ocean floor since they provide insight on many of the Earth's geological, oceanographical, and ecological cycles and processes (*Wessel*, 2007). From a geological perspective, seamounts are particularly important because they are windows into the composition and temperature of the mantle (*Koppers and Watts*, 2010). Scientists study seamounts to keep track of the changing chemical composition of lava and further understand the eruption process. They can also be used to explain the planet's tectonic evolution since plume-generated seamount chains serve as a record of absolute plate motion (*Morgan*, 1971) (*Müller and Seton*, 2015). From an oceanographic perspective, ocean floor bathymetry has an important effect on ocean circulation: large seafloor features such as ridges and plateaus act as barriers that inhibit deep cold water to mix with the warm water of the ocean surface (*Roden et al.*, 1982). Recent studies suggest that smaller features such as seamounts can also play an important role oceanographically and have a greater influence on circulation which can help

scientists better understand the uptake of heat and carbon dioxide in the ocean (*Jayne et al.*, 2004). From an ecological perspective, seamounts are centers for diverse biological communities. The ocean upwelling due to the presence of seamounts brings valuable nutrients from the deep water to the surface. This allows them to become the ideal habitat for fish and a variety of oceanic flora and fauna (*Rogers*, 1994; *Price and Clague*, 2002). Due to the impact that seamounts have on the ocean and ecosystems, they are important features to study, map, and classify.

1.2   Mapping Seamounts

There are two main approaches for mapping seamounts: topographic mapping by multibeam sonar on ships and gravity field mapping by satellite altimetry. Multibeam sonar mapping by oceangoing research vessels provides high resolution bathymetric data (100-200 m) (*Epp and Smoot*, 1989), although a great amount of the ocean (nearly 80 percent) remains unmapped because of the large gap between ship tracks (*Mayer et al.*, 2018). The majority of research surveys have been near mid-ocean ridges for the characterization of small seamounts that formed on young lithosphere (*Wessel et al.*, 2010). Swath surveys in remote areas or along transit cruises commonly map only the flanks of a seamount, so its height is poorly known (*Wessel et al.*, 2010). Complete multibeam coverage of the global seafloor is time-consuming and expensive (*Vogt and Jung*, 2000), so scientists have turned to satellite altimetry to obtain a low-resolution (about 6 km) but global mapping.

Previous studies have shown that gravitational anomalies, derived from satellite altimetry, can be used to find larger seamounts (greater than 2 km tall) (*Lazarewicz and Schwank*, 1982; *Watts and Ribe*, 1984; *Craig and Sandwell*, 1988; *Wessel*, 1997). Satellite altimeters measure the geoid height which, through Laplace's equation, can be converted to deflections of the vertical, gravity anomalies, or vertical gravity gradient (VGG) (*Sandwell and Smith*, 2009). There are four main error sources when detecting and mapping seamounts from satellite-derived anomalies: upward continuation, measurement noise, seafloor roughness, and sediment cover (*Wessel et al.*,
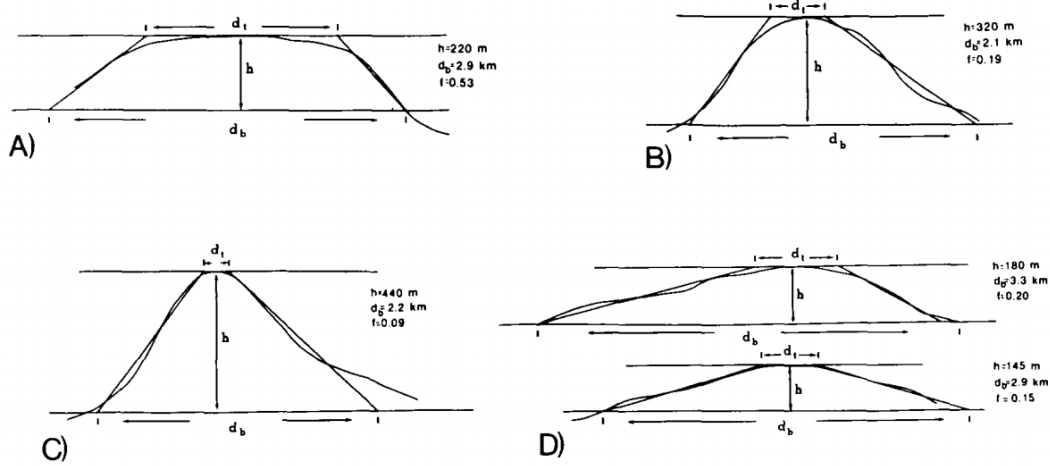
Figure 1.1. The cross-sectional profiles of four small seamounts (*Smith*, 1988), where h is the seamount height, d_b is the basal diameter, and d_t is the diameter of the flattened summit. Flatness, f, is defined by dt/d_b while the height to basal radius ratio is defined by $2h/d_b$.

2010). (1) Upward continuation causes seamounts with diameters less than the mean ocean depth (about 4 km) to be smoothed and attenuated. (2) Ocean waves and currents introduce noise in the satellite altimeter measurements so short wavelength gravity anomalies (less than 20 km) are oftentimes not recovered (*Garcia et al.*, 2014). (3) There are a number of features that contribute to small scale gravity anomalies, including abyssal hills and ridges, and their signals can be confused with those of seamounts. (4) Lastly, older small seamounts are oftentimes covered by sediment on the seafloor. The gravity anomaly will still appear above the buried seamount even though it is not visible in the topography (*Sandwell et al.*, 2014).

Detection and mapping of smaller seamounts (less than 2 km) has relied on multibeam surveys. In a study conducted by Smith (1988), multibeam (SeaBeam) data of 85 seamounts from the Pacific Ocean were analyzed. Smith (1988) found that there is a relatively uniform base radius to height (h) of 0.21, although there are variations in shape and flatness (Figure 1.1). Large seamounts, for example, had smaller flatness values defined by $f = d_t/d_b$, where d_t is the summit diameter and d_b is the basal diameter (*Smith*, 1988). It was also found that the slope angle, defined by $\Phi = arctan(\varepsilon)$ where $\varepsilon = 2h/(d_b - d_t)$, is equal to about 15 degrees (*Smith*,

1988). As seamount height decreases, the flatness generally increases. Small seamounts are much flatter and have a slope angle proportional to summit height (*Smith*, 1988).

1.3   Detecting Seamounts in Satellite Altimetry

Satellite altimetry is a valuable tool for estimating global topography at relatively low spatial resolution (about 6 km) and helping scientists find medium to large seamounts. The first global seamount maps were created from Seasat altimeter profiles. Seasat was launched in 1978 and collected sea surface profiles for just 105 days, which resulted in diamond shaped data gaps with dimensions of 100 km (*Marsh and Martin*, 1982). The analysis of Seasat altimetry profiles was able to identify 8556 seamounts using Gaussian-shaped modeling (*Craig and Sandwell*, 1988). They also found that satellite altimetry can be used to determine the along- track locations of seamount centers with an accuracy of better than 10 km, but the cross-track location was more poorly determined due to the wide track spacing. Another measurable characteristic is the diameter of the seamount, which is equal to the distance between the peak and trough of the along-track vertical deflection (i.e., sea surface slope) profile. This study was able to use the locations of the seamounts to draw conclusions on the global distribution of seamounts. It found that the density of seamounts in the Pacific is higher than the Atlantic or Indian oceans and seamounts preferentially occur on the younger side of large fracture zones (*Craig and Sandwell*, 1988).

Since the Seasat mission, there have been a number of altimeter missions that have greatly improved the accuracy and coverage of the gravity field. This has enabled the construction of the VGG, which is the spatial derivative of the gravity field (*Rummel and Haagmans*, 1990). This spatial derivative amplifies short wavelengths and suppresses long wavelengths so it is a valuable tool for locating smaller features on the ocean floor (*Kim and Wessel*, 2011). However, the spatial derivative also amplifies short wavelength noise, which limits seamount detectability. The recently released VGG version has significantly lower noise levels because of new altimeter

data from the CryoSat-2, Envisat, and Jason-1 missions (*Sandwell et al.*, 2014). After comparing the old and new VGG published in 2015, it was found that the signal to noise ratio (SNR) has increased about 48 percent, indicating that multiple altimetry sources can improve gravity data and help find unmapped features on the ocean floor. Over the past 5 years, there have been additional advances in SNR, so many more seamounts are apparent in the VGG.

For our study, we used version 30 of the vertical gravity gradient to expand the global seamount catalog and then model the typically radially-symmetric morphology of seamounts (*Sandwell et al.*, 2021). We hope to be able to use their characteristic shapes to improve the resolution of seafloor bathymetry despite limited data availability from multibeam sonar.

Chapter 2

Data Preparation

To begin the investigation, we constructed high resolution VGG images for Google Earth that allowed for the visualization of seamounts as well as already-digitized tectonic features. The data sets used in Google Earth included the vertical gravity gradient (VGG) (*Sandwell et al.*, 2021), digitized ridges and seesaw-propagators (*Matthews et al.*, 2011; *Wessel et al.*, 2015), global bathymetry and topography through the use of SRTM15+V2.3 (*Tozer et al.*, 2019), and previous seamounts picked by Kim and Wessel (2011).

2.1   Updating the Kim-Wessel Seamount Catalog

In 2011, Kim and Wessel were able to find 24,643 potential seamounts located away from continental margins using the VGG. Although they indicated that a majority of the planet's seamounts are less than 1 km tall, their count for small seamounts was limited due to attenuated gravity signals and upward continuation. As the VGG grids are updated, smaller uncharted seamounts are better resolved.

To update this Kim-Wessel catalog, we used the newly refined VGG (Version 30), which revealed many smaller seamounts as well as resolving individual seamounts along ridges. In order to choose new locations, we divided the Earth into 30 degree longitude by 30 degrees latitude cells which we then examined one at a time. We identified new seamounts by eye, avoiding seafloor features such as fracture zones, transform faults, ridge axes, and see-saw
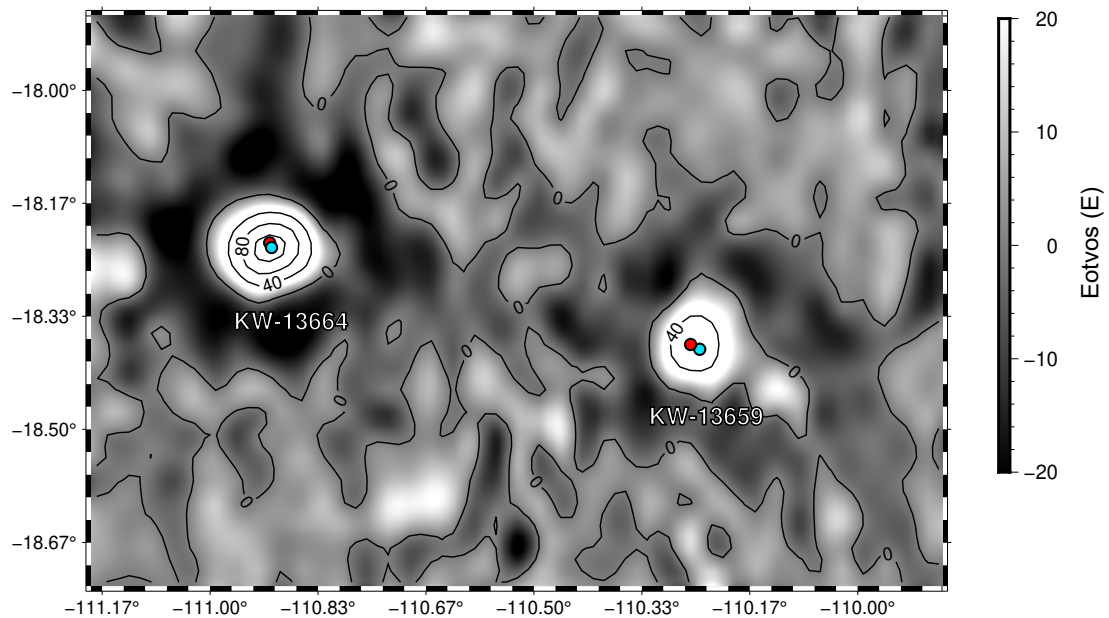
Figure 2.1. Two seamounts from the Kim-Wessel catalog before and after being centered (20 Eotvos contours). Light blue colored points indicate the original location of the seamounts. Red points are the new centers chosen based on the maximum VGG value.

propagators since these can give signals that may look like seamounts in the VGG. Through this method we were able to identify 10,794 new seamounts, expanding the catalog by one third. The new VGG also helped us find 514 seamounts that were misidentified in the Kim-Wessel catalog of 24,643 (2011). This included any seamount picks that no longer showed a gravity signal in the VGG. After removing these and finalizing the new picks, the updated catalog came to a total of 34,923 seamounts.

The next step was to recenter all of the seamount picks using Python and the "grdtrack" module from the generic mapping tool GMT (*Wessel et al.*, 2019). To do this, we searched for the maximum VGG in a 5x5 pixel (about 5 minute) area around the initial seamount pick. Although the location of the maximum in the VGG is oftentimes not the exact geometric center of the seamount, it is a good reference to use for modeling (Figure 2.1).

8

2.2 Refining the Sample

After the central longitude and latitude were found, we filtered the catalog for well-charted seamounts (i.e., those having at least 50 percent multibeam sonar coverage of the seamount and complete coverage of its summit). This search was accomplished by using the source identification grid associated with the SRTM15+V2.3 global bathymetry (*Tozer et al.*, 2019). This process resulted in 739 well-charted seamounts less than 2500 m tall; 554 from the Kim-Wessel catalog and 185 from the new catalog. An example of a seamount with good data coverage is shown in Figure 2.2. For each well-mapped seamount, we calculated the base depth and maximum seamount height. The base depth was taken as the median depth on a 30 km by 30 km area surrounding the center of the seamount. Seamounts are surrounded by relatively flat seafloor, so this base depth is well defined by the median of the depth histogram (Figure 2.2c). The maximum seamount height above the base depth was derived from the shallowest depth in the same area (i.e. summit depth - base depth) (Figure 2.2d). It is important to note that the maximum seamount height is the shallowest point on the seamount and not necessarily the height at the VGG centered location.

2.3 Empirical Orthogonal Function Analysis

An empirical orthogonal function (EOF) analysis allows for the finding of patterns within a specific data-set by using matrices and their corresponding eigenvalues. We use the EOF analysis (*Preisendorfer and Mobley*, 1988; *Hannachi et al.*, 2007) to seek the basic structure of the 739 well-charted seamounts. For each seamount, we divide the height and the radius by the maximum height to get the normalized height and normalized radius. We sample the seamounts at fixed normalized radii (0 to 12.5 at 0.5 spacing) and construct a $M \times N$ two-dimensional matrix of the normalized heights at fixed normalized radii, where M is 739 (the number of seamounts) and N is 26 (the number of radius points). Figure 2.3 shows the first three modes of the analysis. Since the first mode of EOF analysis explains 90.8 percent of the total variance, we can neglect all

other modes. Its expansion coefficients, which represent the structures in the sampling dimension, resemble a Gaussian shape. Based on this result, we assume that each seamount has a radial symmetrical Gaussian shape and a common base to height ratio (i.e. amplitude divided by the standard deviation in Gaussian function). We then use two methods to compute this base to height ratio: an average Gaussian fit to the sample of 739 seamounts and an individual Gaussian fit for each seamount in the sample.
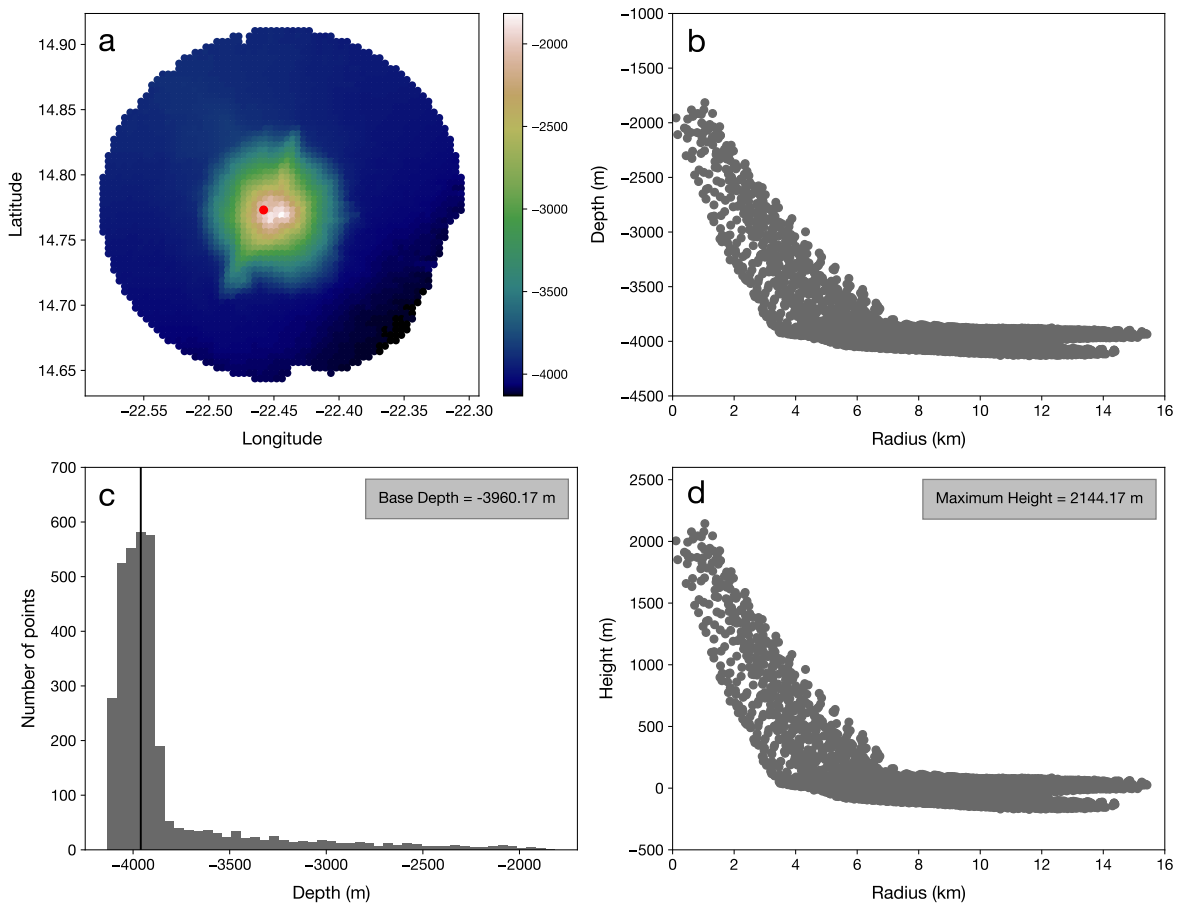

Figure 2.2. (a) and (b) Seamount KW-00648 depth data within a 15 km radius. The red dot indicates the VGG center of the seamount. (c) A histogram is used to find the base depth. (d) The heights of the data points shifted by base depth.
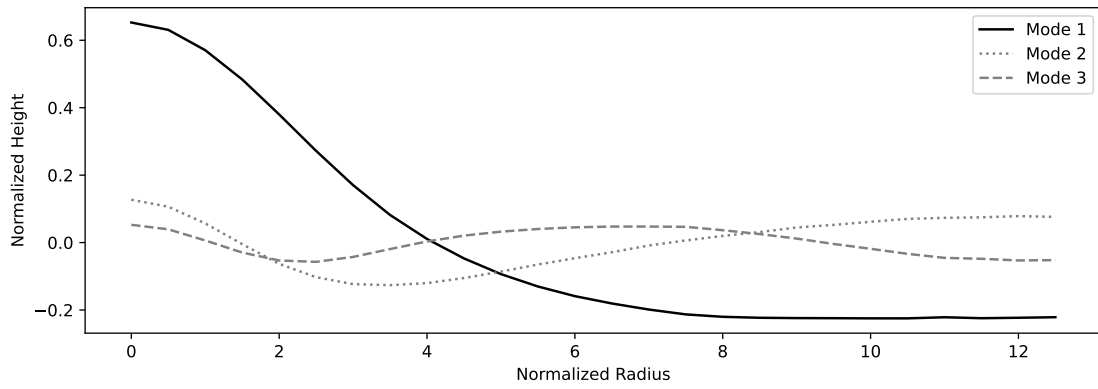
Figure 2.3. Three Modes of the EOF analysis where Mode 1 resembles a Gaussian shape and explains 90.8 percent of the variance.

Chapter 3

Modeling Seamounts

3.1 Method 1: Average Gaussian Fit

To prepare for the average Gaussian fit, the height above the base depth for each seamount, as well as the radius, were normalized by the maximum height. The normalized height was then median-filtered at 0.5 normalized radius increments using the "filter1d" function in GMT. We then combined the radially normalized height data from all seamounts to obtain the median normalized heights and median absolute deviation. This data was then fit to the following Gaussian equation

$$y_d = h \exp(\frac{-r^2}{2\sigma^2}) + y_o \tag{3.1}$$

where r is the seamount normalized radius from 0 to 12.5 with a 0.5 spacing, h is the height, σ is the characteristic width, and y_o is adjusted base depth. This analysis used the median normalized heights for y_d and median-absolute deviation as the error associated to find the h and σ through least square fitting. Since this analysis is done with a profile stack of all the seamounts where the normalized median height converges to zero at larger radii, y_o is set to zero.

This three-parameter Gaussian model produces the best-fitting height and characteristic width of our collective seamounts (Table 3.1). Our model had a σ/h equal to 2.4 with a maximum absolute slope of 0.25 and explained around 99 percent of the variance (Figure 3.1).
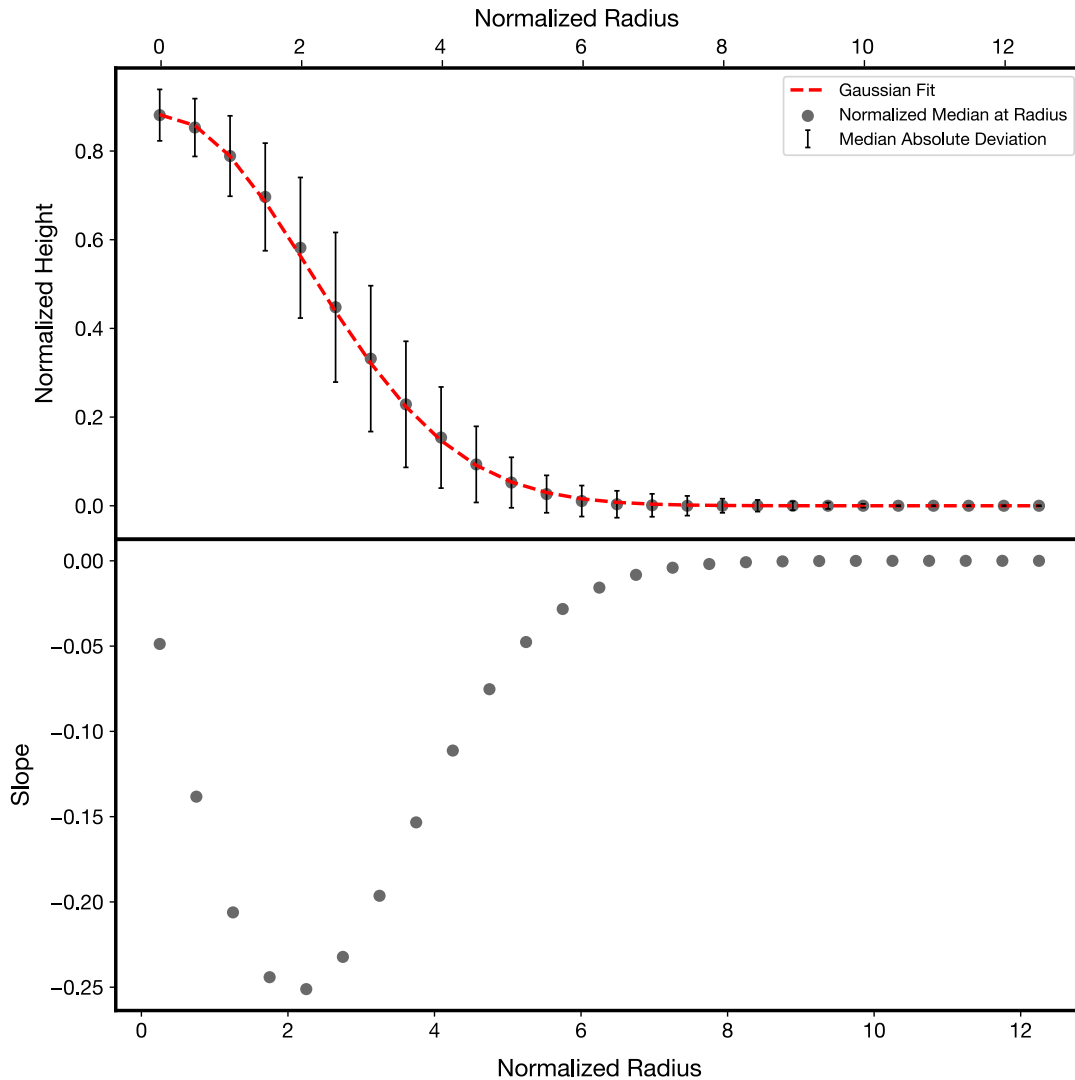
Figure 3.1. (top) Best fit Gaussian model versus normalized radius has a $\sigma/h = 2.4$ (red dashed line); medium value of normalized height (gray dots) and the associated median absolute deviation (gray error bar) versus normalized radius. Note that the normalized height on the *y*-axis is less than 1 because VGG centering does not always define the maximum height of the seamount as the center. (bottom) Slope of the Gaussian model has a maximum absolute value of 0.25.

Figure 3.2. For each seamount example, (left) SRTM15+V2.3 mapped bathymetry, (center) the average Gaussian Model where $\sigma/h = 2.4$, (right) difference between the average Gaussian model and real data. The gray areas have no soundings. a) New-08100. b) KW-00783. c) KW-00648. d) KW-15253. e) KW-00543. f) KW-16423.
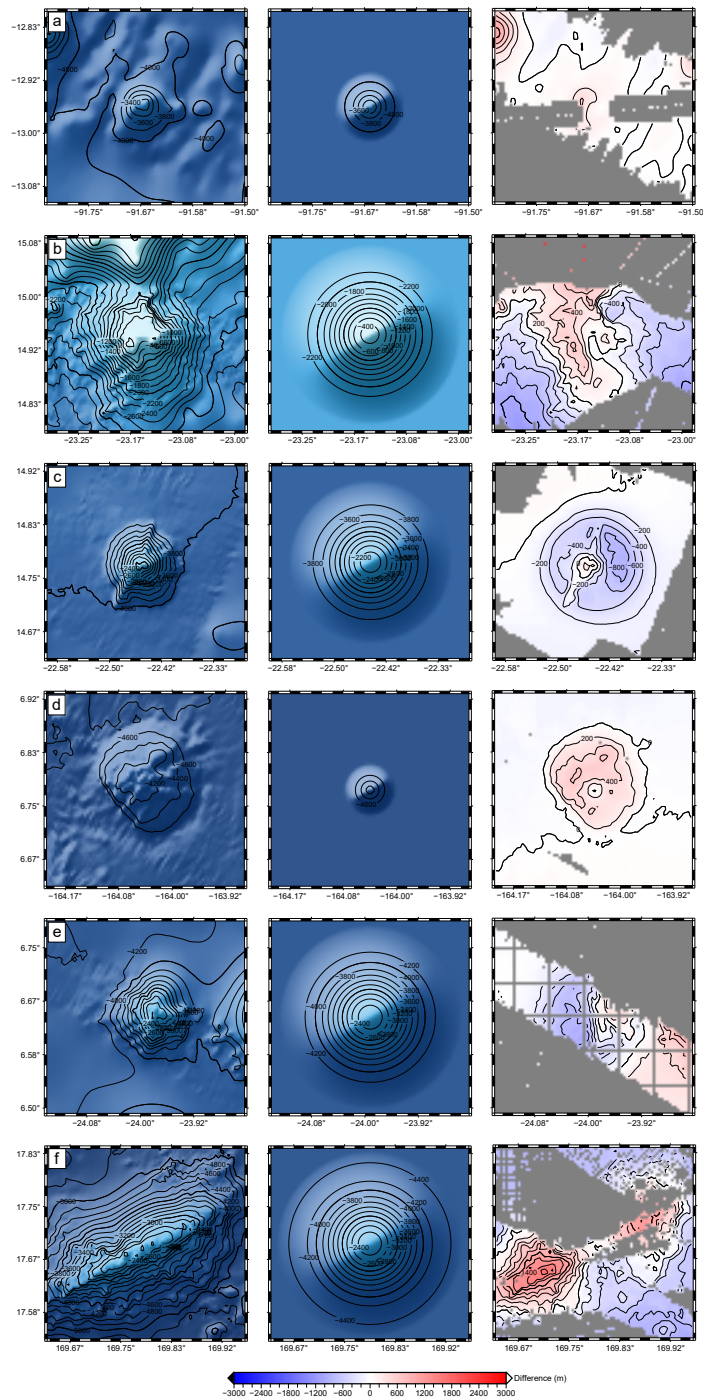
Table 3.1. The results from tests run on both the Kim-Wessel seamounts and New seamounts separately in addition to a collective analysis denoted by All.

	Number of Seamounts	Height h	Sigma σ	σ/h	Absolute Slope	Fraction of Variance Explained (Gaussian Fit)	Fraction of Variance Explained (EOF)
Kim-Wessel	544	0.88303	2.10605	2.3850	0.2520	99%	89.9%
New	185	0.84944	1.97007	2.2015	0.2726	99%	90.8%
All	739	0.88199	2.11224	2.3948	0.2511	99%	90.29%

The maximum absolute slope of the best-fit model is in good agreement with a previous study based on the analysis of 88 seamounts where the seamount height was one fifth of the basal radius (*Smith*, 1988). The final ratio between sigma and height, σ/h, with a value of about 2.4 is important in defining the final model, and ultimately, the gravity field of the Gaussian seamount that is used to construct a new global synthetic bathymetry (SYNBATH) where this factor is used to sharpen the shapes of predicted seamounts (*Sandwell et al.*, 2022).

To evaluate the model, we applied the average Gaussian model to each seamount and computed the difference between topography extracted from the SRTM15+V2.3 and the Gaussian model created using the "grdseamount" function in GMT. GMT "grdseamount" takes the central longitude, central latitude, model height, and radius (3 σ) as input. We used the median height at the summit of the seamount for the model height. This value is determined by filtering the real data in 0.5 km median increments and finding the maximum. Using the median height at the summit instead of the maximum height allows for less error in the fitting of the model that might have occurred due to singular sharp peaks at the summit. We examined the model fits to all 739 seamounts but only 6 are plotted in Figure 3.2 to illustrate some good fits, as well as cases where the fits are poor. (a) New-08100 is a small seamount with a height of 933 m. The misfit (right) has a scale of ±143 m and a 200 m contour interval. (b) KW-00783 shows a good fit for a large seamount with a height of 2099 m. (c) KW-00648 shows an overestimated model fit. In this case, the seamount is narrower than the model. (d) KW-15253 shows an underestimated model. Here, the seamount is wider than the model. (e) KW-00543 shows the results from a poorly centered seamount. (f) KW-16423 shows the result of an elliptical seamount that is poorly fitted by a radial Gaussian model.

3.2   Method 2: Individual Gaussian Fit

Since the first method has several seamounts with poor fits, we re-did the analysis by fitting a Gaussian model to each seamount individually. To test which set of seamount height

series data is best for this fitting, we compared three types of data: all available bathymetric data, GMT "filter1d" calculated median heights from radii 0-12.5 km, and GMT "filter1d" calculated robust median heights from radii 0-12.5 km. The results showed that the median and robust median had better fits than the model using all available bathymetric data, but produced very similar results. Because of this, we chose to use the robust median height data for the second analysis. The robust median height data y_d and radius r input data (unit of km) are fit to equation 3.1. Each seamount then receives its own unique h, σ, and y_o values, which are height, sigma, and adjusted base depth respectively. Figure 3.3 shows an example of an individual fit for seamount New-00842 in two dimensions.
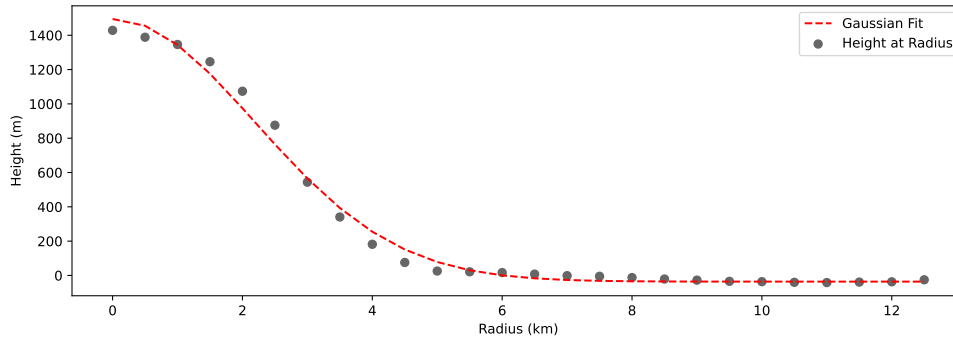

Figure 3.3. Individual Gaussian fit (red dashed line) of seamount New-00842 to height at radius (grey dots) where $h = 1530.64$ m, $\sigma = 2.19$, and $y_d = 35.92$ m. By using this sigma value, we obtain a radius of 6.58 km.

In Figure 3.4 we have modeled the same 6 seamounts with GMT "grdseamount" as before but with their individual Gaussian fitting. The median of the σ/h ratio for these 739 individually fitted seamounts had a value of 2.39 and a mean of 2.6 (Figure 3.5). This matches well with the value we obtained from the first approach, indicating that the average seamount fitting and ratio of about 2.4 is a good representation of the morphology of the majority of small seamounts.

17
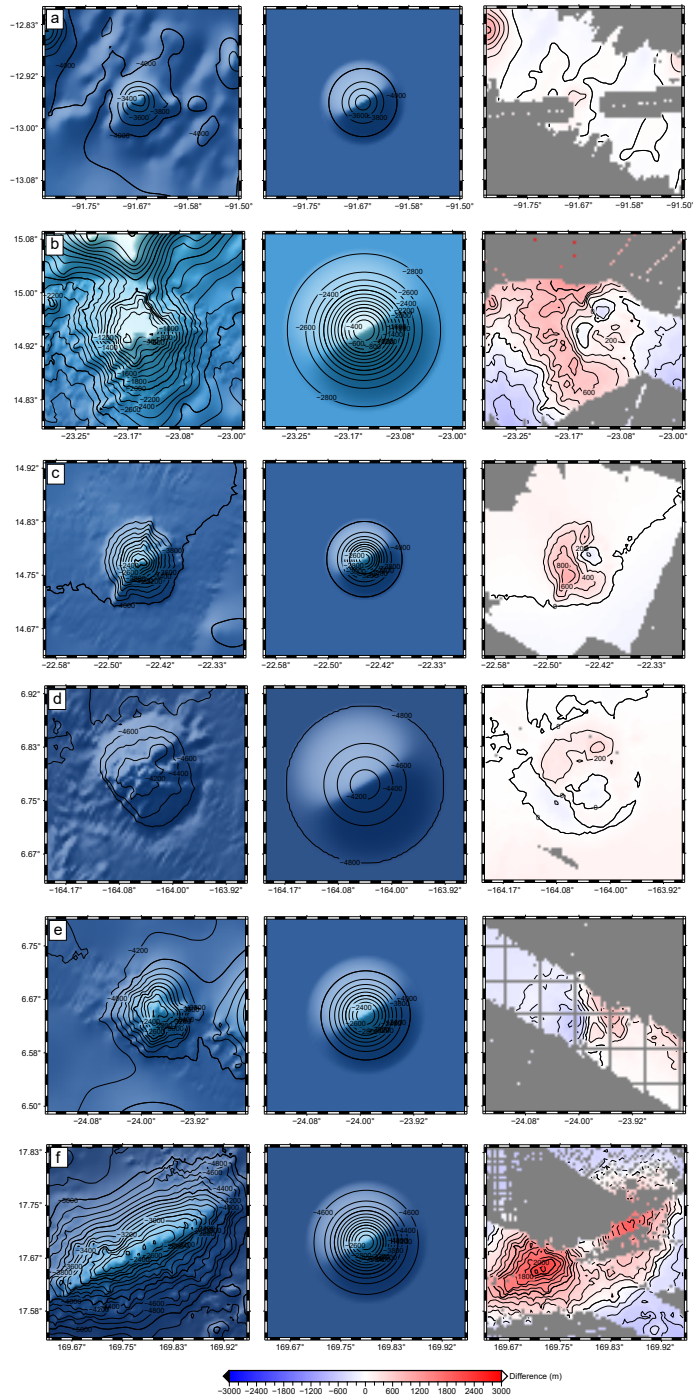
Figure 3.4. For each seamount example, (left) SRTM15+V2.3 mapped bathymetry, (center) the individual Gaussian model where σ/h is unique to each seamount, (right) difference between the individual Gaussian model and real data. a) New-08100. b) KW-00783. c) KW-00648. d) KW-15253. e) KW-00543. f) KW-16423.
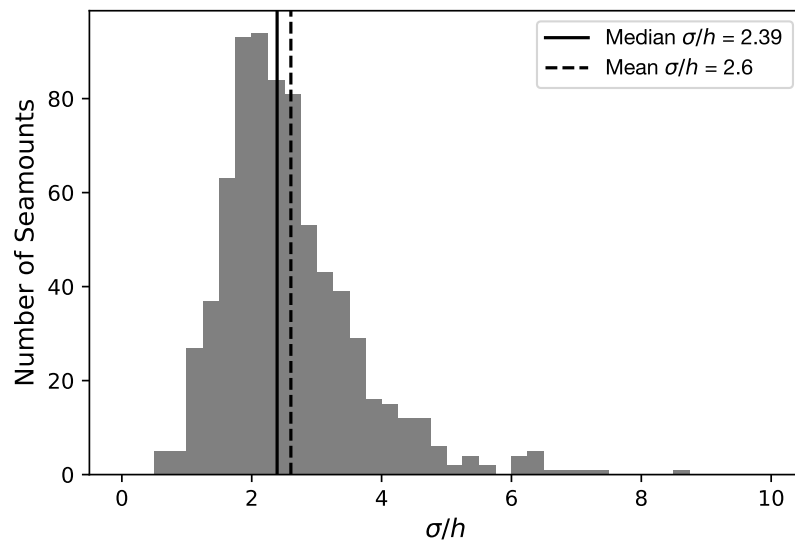
18

Figure 3.5. σ/h ratios for the 739 seamounts plotted as a histogram. The median value is 2.39 and mean is 2.6.

Chapter 4

Discussion

4.1   Comparing Heights from both Methods

The relationships between maximum height and model height from Method 1 and Method 2 respectively have been plotted below. Figure 4.1a shows that the relation between the maximum and model height is linear and therefore, the model serves as a good representation of the seamount height used for the Gaussian analysis. The model height is always less than or equal to the maximum height because the data that we used is filtered with GMT "filter1d" from 0-12.5 radii in 0.5 intervals. Each radius would have the median height value, which would naturally decrease the height value from the maximum height. Figure 4.1b shows the values for h height obtained through the individual Gaussian fit against the maximum height of the seamount. Although this graph shows more variability in the data, it generally still follows a linear trend.

4.2   Comparing RMS Error from both Methods

The root mean square (RMS) error is calculated from the difference of the model and real topography data available within a 30 by 30 km area. When comparing the results of the average (Figure 3.2) and individual (Figure 3.4) fitting of these six example seamounts we can see interesting results. From this sample, five of the six seamounts showed a better fit through Method 2. As shown in Table 2 below, we can see that the RMS for all but seamount KW-16423 decreased in error. This is understandable since seamount KW-16423 is elliptical and would not

well fit a radially symmetric Gaussian model regardless of the method. For seamounts such as this case, additional parameters such as ellipticity would need to be added for more accurate modeling (*Kim and Wessel*, 2011).
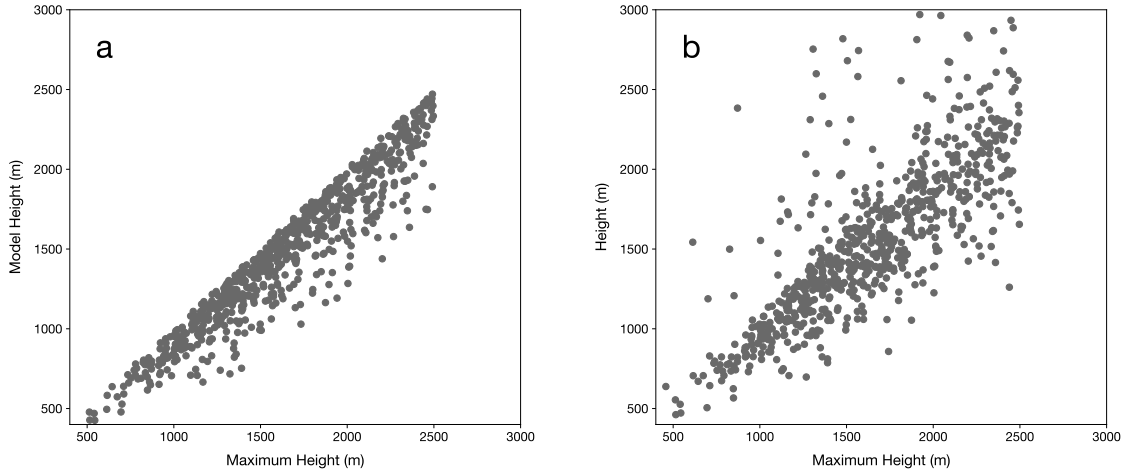

Figure 4.1. (a) Heights from Method 1 plotted against the maximum heights of the seamounts. (b) Heights Method 2 plotted against the maximum heights of the seamounts.

Table 4.1. The RMS misfits of the six seamounts from Method 1 and 2 calculated from Figure 3.2c and 3.4c. Units are in meters (m).

	Method 1 RMS	Method 2 RMS
New-08100	±143.19	±139.75
KW-00543	±380.53	±266.70
KW-00648	±213.57	±160.80
KW-00783	±546.14	±436.32
KW-15253	±155.85	±78.05
KW-16423	±603.80	±698.40

The RMS misfits of all 739 seamounts from both methods are shown in Figure 4.2. The Average Gaussian fit method shows a slightly wider range in RMS misfit distribution. In contrast, the Individual Gaussian fit method RMS has less variation as the height increases. For both methods however, we see that RMS misfit increases as seamount height increases. This indicates that the height error is typically 20 percent of the seamount height as shown by the line in Figure
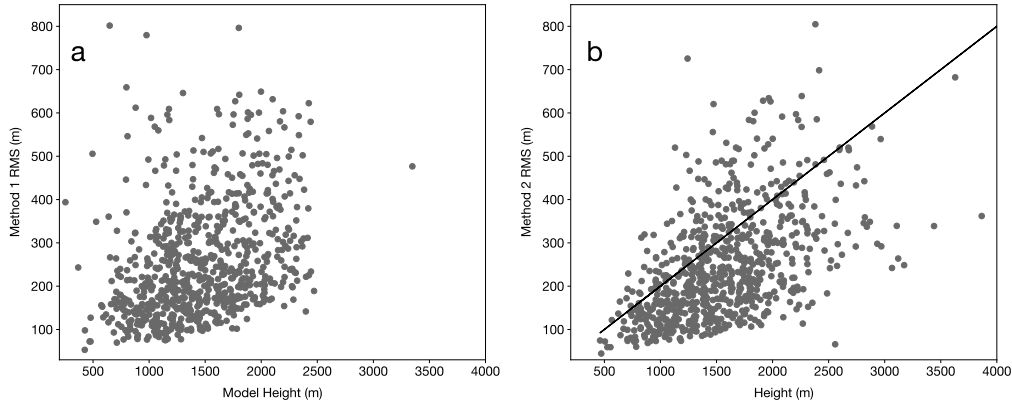
Figure 4.2. (a) Method 1 Model Heights of seamounts plotted against their RMS. (b) Method 2 heights plotted against each corresponding model RMS.

4.2b.

When comparing the values directly, 454 seamounts showed improvement in the misfit after Method 2, while the other 285 had more error. The RMS misfit of the 454 seamounts improved by a median value of -38.65 m, while the RMS misfit of the 285 diminished by a median value of 34.03 m. This shows that modeling seamounts individually through Method 2 serves as a better tool than Method 1.

4.3 Comparing Our Gaussian Model with Smith (1988)

In Smith (1988), 85 seamounts were analyzed based on their height to base radius ratios (more on her method in Chapter 1.2). In that study, Smith used a flattened cone model as seen in Figure 1.1 rather than a Gaussian model. It is important to note that she defined flatness values as $f = d_t/d_b$, where d_t is the summit diameter and d_b is the basal diameter. Through her analysis, it was found that the seamounts' summit height is about one fifth of the basal radius, with a ratio of 0.21.

In order to compare the height to base ratio of our own analysis to that of Smith's, we fit a flattened cone model to our average Gaussian model. First, we created a 1000 km tall Gaussian seamount where $\sigma/h = 2.4$ using GMT "grdseamount." We then made several flattened

cone seamounts, all of which were 1000 km tall, but varied their sigma values by 0.1. GMT "grdseamount" allows the user to input a flatness value, f. In Smith's study, a 17-point sample mean of seamounts (1000 to 1800 km tall) had a flatness value of 0.22 ± 0.11. Because of this, we use $f = 0.22$ for our flattened cone models. The smallest RMS error obtained from the difference between the Gaussian model and flattened cone models allows us to find the sigma equivalent for Smith's analysis (Figure 4.3). Through this method, we determine that h/r_b described by Smith (1988) is approximately the same as $h/2.1\sigma$ (Table 4.2). The height to base ratios of the 739 seamounts from our sample and the 85 seamounts described by Smith (1988) are shown in Figure 4.4.

Table 4.2. Comparison of height to base radius ratios from the Smith analysis (1988) and this study.

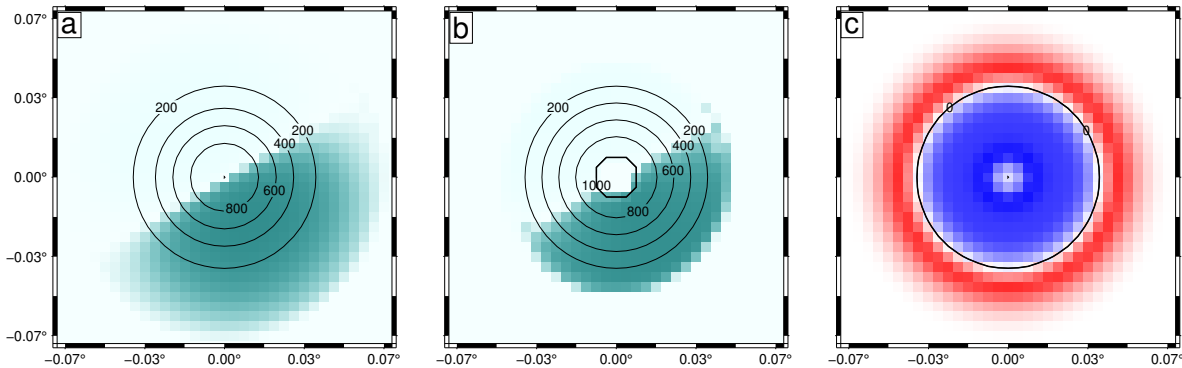|	85 Seamounts (*Smith*, 1988)	739 Seamounts (this study)
Height to Base Radius ratios	$h/r_b = 0.21$	$h/2.1\sigma = 0.198$

Figure 4.3. (a) Gaussian seamount where $\sigma = 2.39$ (b) Conical seamount where $f = 0.22$ and $r_b = 2.1\sigma$ (c) Difference between (a) and (b) with an RMS of 19.42 m.
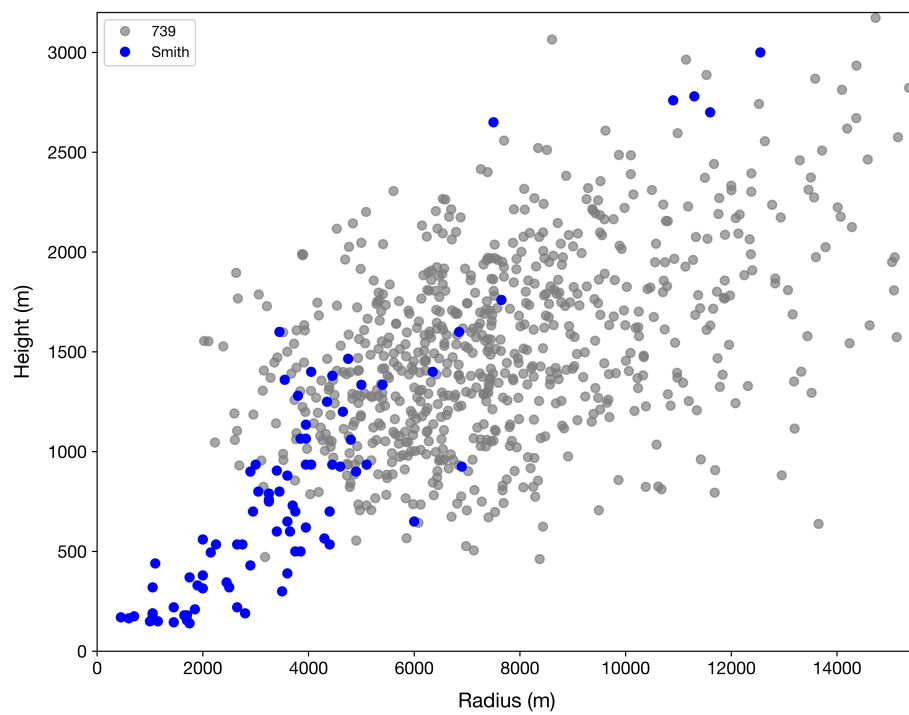
Figure 4.4. Height vs. base radius of 85 Smith (1988) and our 739 seamounts based on height data from Method 2.

Chapter 5

Conclusion

The vertical gravity gradient and the methods of Gaussian modeling can allow for clarity in understanding the morphology of globally distributed seamounts. Improvement in the VGG allowed us to expand the Kim-Wessel (2011) catalog by 10,794 seamounts. The addition of these new seamounts and refinement of previous picks updated the catalog to a total of 34,923 seamounts. We were then able to model them using two methods to show that medium sized seamounts have a characteristic σ/h of 2.4 and an equivalent height to base ratio of about 0.20. This is in good agreement with an earlier study by Smith (1988), who found that the summit height is around one fifth of the basal radius. Our methods indicate that the VGG can be used to estimate the height of small seamounts to an accuracy of about 270 m.

Although our models provide a good representation of seamount shape, the radially symmetric Gaussian model has significant deviations from actual seamount shape. The way in which the center of the seamount is chosen can also have an effect on the model. It is common that the highest point of the seamount does not correspond to either the largest vertical gravity gradient signal or its geometric center. When comparing the RMS misfit of both Gaussian Model methods, the individual seamount modeling method shows less error. However, both indicate that the error in modeling increases as seamount height increases.

Our Individual Gaussian model was based on three parameters: height (h), characteristic width (σ), and adjusted base depth (y_o). Including additional parameters such as ellipticity in

future analyses can help account for the shape of some seamounts when modeling and provide a better fit. Prospective improvements in the VGG can further expand our knowledge of seamounts and their role on the planet while surveying done by multibeam sonar remains limited.

This thesis, in part, has been submitted for publication of the material as it may appear in Earth and Space Science, 2022, Gevorgian, Julie; Sandwell, David T.; Yu, Yao; Kim, Seung-Sep; Wessel, Paul. The thesis author was the primary investigator and author of this paper.

Bibliography

Batiza, R. (1981), Lithospheric age dependence of off-ridge volcano production in the north pacific, *Geophysical Research Letters*, *8*, 853–856.

Craig, C. H., and D. T. Sandwell (1988), Global distribution of seamounts from seasat profiles, *Journal of Geophysical Research*, *93*, 10,408–10,420.

Epp, D., and C. Smoot (1989), Distribution of seamounts in the north atlantic, *Nature*, *337*, 254–257.

Fryer, P. (1996), Evolution of the mariana convergent plate margin system, *Reviews of Geophysics*, *34*, 89–125, doi:10.1029/95RG03476.

Garcia, E. S., D. T. Sandwell, and W. H. Smith (2014), Retracking cryosat, envisat and jason-1 radar altimetry waveforms for improved gravity field recovery, *Geophysical Journal International*, *196*, 1402–1422.

Hannachi, A., I. T. Jolliffe, and D. B. Stephenson (2007), Empirical orthogonal functions and related techniques in atmospheric science: A review, *International Journal of Climatology*, *27*, 1119–1152.

Jayne, S. R., L. C. S. Laurent, and S. T. Gille (2004), Special issue-bathymetry from space connections between ocean bottom topography and earth's climate, *Oceanography*, *17*.

Kim, S. S., and P. Wessel (2011), New global seamount census from altimetry-derived gravity data, *Geophysical Journal International*, *186*, 615–631, doi:10.1111/j.1365-246X.2011.05076.x.

Koppers, A., and A. Watts (2010), Intraplate seamounts as a window into deep earth processes, *Oceanography*, pp. 42–57.

Lazarewicz, A. P., and D. C. Schwank (1982), Detection of uncharted seamounts using satellite altimetry, *Geophysical Research Letters*, *9*, 385–388.

Marsh, J. G., and T. V. Martin (1982), The seasat altimeter mean sea surface model, *Journal of*

Geophysical Research, *87*, 3269, doi:10.1029/jc087ic05p03269.

Matthews, K. J., R. D. Mller, P. Wessel, and J. M. Whittaker (2011), The tectonic fabric of the ocean basins, *Journal of Geophysical Research: Solid Earth*, *116*, doi:10.1029/2011JB008413.

Mayer, L., M. Jakobsson, G. Allen, B. Dorschel, R. Falconer, V. Ferrini, G. Lamarche, H. Snaith, and P. Weatherall (2018), The nippon foundation-gebco seabed 2030 project: The quest to see the world's oceans completely mapped by 2030, *Geosciences (Switzerland)*, *8*, doi: 10.3390/geosciences8020063.

Menard, H. W. (1964), *Marine Geology of the Pacific*, McGraw Hill.

Morgan, W. J. (1971), Convection plumes in the lower mantle, *Nature*, *230*, 42–43, doi:10.1038/230042a0.

Müller, D., and M. Seton (2015), *Plate Motion*, 1-10 pp., Springer, doi:10.1007/978-94-007-6644-0_131-1.

Preisendorfer, R. W., and C. D. Mobley (1988), *Principal Component Analysis in Meteorology and Oceanography*, Elsevier.

Price, J. P., and D. A. Clague (2002), How old is the hawaiian biota? geology and phylogeny suggest recent divergence, *Proceedings of the Royal Society B: Biological Sciences*, *269*, 2429–2435, doi:10.1098/rspb.2002.2175.

Roden, G. I., B. A. Taft, and C. C. Ebbesmeyer (1982), Oceanographic aspects of the emperor seamounts region., *Journal of Geophysical Research*, *87*, 9537–9552, doi:10.1029/JC087iC12p09537.

Rogers, A. D. (1994), The biology of seamounts, *Advances in Marine Biology*, *30*, 305–350, doi:10.1016/S0065-2881(08)60065-6.

Rummel, R., and R. H. Haagmans (1990), Gravity gradients from satellite altimetry, *Marine Geodesy*, *14*, 1–12, doi:10.1080/15210609009379641.

Sandwell, D. T., and W. H. Smith (2009), Global marine gravity from retracked geosat and ers-1 altimetry: Ridge segmentation versus spreading rate, *Journal of Geophysical Research: Solid Earth*, *114*, doi:10.1029/2008JB006008.

Sandwell, D. T., R. D. Müller, W. H. Smith, E. Garcia, and R. Francis (2014), New global marine gravity model from cryosat-2 and jason-1 reveals buried tectonic structure, *Science*, *346*, 65–67, doi:10.1126/science.1258213.

Sandwell, D. T., H. Harper, B. Tozer, and W. H. Smith (2021), Gravity field recovery from

geodetic altimeter missions, *Advances in Space Research*, *68*, 1059–1072, doi:10.1016/j.asr. 2019.09.011.

Sandwell, D. T., J. A. Goff, J. Gevorgian, H. Harper, S. S. Kim, Y. Yu, B. Tozer, P. Wessel, and W. H. Smith (2022), Improved bathymetric prediction using geological information: Synbath, *Earth and Space Science*, *9*, doi:10.1029/2021EA002069.

Smith, D. K. (1988), Shape analysis of pacific seamounts, *Earth and Planetary Science Letters*, pp. 457–466.

Smith, D. K., and J. R. Cann (1990), Hundreds of small volcanoes on the median valley floor of the mid-atlantic ridge at 24-30 n., *Nature*, pp. 152–155.

Smith, D. K., and T. H. Jordan (1988), Seamount statistics in the pacific ocean, *Journal of Geophysical Research*, *93*, 2899, doi:10.1029/jb093ib04p02899.

Staudigel, H., A. A. Koppers, J. W. Lavelle, T. J. Pitcher, and T. M. Shank (2010), Defining the word "seamount", *Oceanography*, *23*, 20–21, doi:10.5670/oceanog.2010.85.

Tozer, B., D. T. Sandwell, W. H. Smith, C. Olson, J. R. Beale, and P. Wessel (2019), Global bathymetry and topography at 15 arc sec: Srtm15+, *Earth and Space Science*, *6*, 1847–1864.

Vogt, P. R. (1974), Volcano spacing, fractures, and thickness of the lithosphere, *Earth and Planetary Science Letters*, *21*, 235–252.

Vogt, P. R., and W.-Y. Jung (2000), Gomap: A matchless resolution to start the new millennium, *Eos, Transactions American Geophysical Union*, *81*, 254, doi:10.1029/00EO00180.

Watts, A. B., and N. M. Ribe (1984), On geoid heights and flexure of the lithosphere at seamounts., *Journal of Geophysical Research*, *89*, 11,152–11,170, doi:10.1029/JB089iB13p11152.

Watts, A. B., D. T. Sandwell, W. H. Smith, and P. Wessel (2006), Global gravity, bathymetry, and the distribution of submarine volcanism through space and time, *Journal of Geophysical Research: Solid Earth*, *111*, doi:10.1029/2005JB004083.

Wessel, P. (1997), Sizes and ages of seamounts using remote sensing: Implications for intraplate volcanism, *Science*, *277*, 802–805, doi:10.1126/SCIENCE.277.5327.802.

Wessel, P. (2001), Global distribution of seamounts inferred from gridded geosat/ers-1 altimetry, *Journal of Geophysical Research: Solid Earth*, *106*, 19,431–19,441, doi:10.1029/ 2000jb000083.

Wessel, P. (2007), Seamounts: Ecology, fisheries, and conservation, pp. 3–20.

Wessel, P., D. T. Sandwell, and S.-S. Kim (2010), The global seamount census, *Oceanography*, *23*, 24–33.

Wessel, P., K. J. Matthews, R. D. Muller, A. Mazzoni, J. M. Whittaker, R. Myhill, and M. T. Chandler (2015), Semiautomatic fracture zone tracking, *Geochemistry, Geophysics, Geosystems*, *16*, 2462–2472, doi:10.1002/2015GC005853.

Wessel, P., J. F. Luis, L. Uieda, R. Scharroo, F. Wobble, W. H. Smith, and T. D (2019), The generic mapping tools version 6, *Geochemistry, Geophysics, Geosystems*, *20*, 5556–5564.

Wilson, J. T. (1963), A possible origin of the hawaiian islands, *Can. J. Phys. Downloaded from cdnsciencepub.com by*, *41*, 863–870.